Applied Thermal Engineering 264 (2025) 125492

Contents lists available at ScienceDirect

Applied Thermal Engineering

journal homepage: www.elsevier.com/locate/apthermeng

Research Paper

Thermodynamic optimization analysis of a combined cooling and power system integrating a chemical looping combustion with a dual-throttle self-condensing transcritical CO_2 cycle

Yadong Du [a], Ce Yang [a,*], Haimei Wang [a], Weihua Sun [b], Hanzhi Zhang [a,*], Buchen Wu [c,*]

[a] School of Mechanical Engineering, Beijing Institute of Technology, Beijing 100081, China
[b] State Grid Integrated Energy Service Group Co., LTD, Beijing 100052, China
[c] Department of Mechanical and Aerospace Engineering, The Hong Kong University of Science and Technology, Clear Water Bay, Kowloon, Hong Kong China

ARTICLE INFO

Keywords:
Chemical looping combustion
Self-condensing transcritical CO_2 cycle
Dual-throttle
Combined cooling and power
Thermodynamic analysis
Multi-objective optimization

ABSTRACT

The ways of utilizing waste heat from chemical looping combustion (CLC) power generation systems warrant further exploration. In this study, a dual-throttle self-condensing transcritical CO_2 cycle is proposed to recover the waste heat from a copper-based CLC-driven power system, aiming to realize flexible combined cooling and power generation. After establishing the mathematical model, the performance comparisons, exergy analysis, and parametric studies are performed to elucidate the thermodynamic characteristics of the system. Subsequently, a multi-objective optimization is executed for the system to evaluate the cogeneration capacity and determine the optimal design boundary. The results show that the dual-throttle configuration reduces the system's electrical and exergy efficiencies by only 1.25 and 1.15 percentage points, respectively, compared to the power generation-only single-throttle configuration. Among the components, the reactors and regenerators exhibit the highest exergy destruction. Optimization findings reveal that the system's power generation capacity ranges from 24374.36 kW to 26473.26 kW, corresponding to a cooling capacity range of 1386.02 kW to 187.69 kW. Under the optimal trade-off conditions, the system achieves an electrical efficiency of 52.02 %, an exergy efficiency of 50.17 %, and a cooling power output of 1169.08 kW.

1. Introduction

Despite the vigorous advancement of renewable energy sources, fossil fuels continue to dominate the global energy landscape [1]. The significant environmental issues arising from the substantial carbon dioxide (CO_2) emissions associated with fossil fuel combustion underscore the urgent need for effective carbon capture technologies. However, the current carbon capture strategies, including pre-combustion, post-combustion, and oxy-fuel combustion, encounter challenges such as high costs and energy penalties [2,3]. In contrast, chemical looping combustion (CLC) technology offers great prospects and necessity. The CLC technology provides two key advantages: (1) it enhances power generation efficiency by mitigating energy losses typical of conventional combustion processes [4], and (2) it produces only CO_2 and water as combustion byproducts, omitting nitrogen oxides (NO_x), which simplifies the capture process and reduces the associated costs while ensuring efficient CO_2 capture [5]. Furthermore, the adaptability of CLC technology to various fuels such as coal, natural gas, and biomass makes it crucial for advancing clean energy transitions and achieving sustainable development [6].

The CLC technology, characterized by contactless combustion, consists of a fuel reactor, an air reactor, and a solid phase-supported metal oxygen carrier [7]. The oxygen carrier is circulated between the fuel and air reactors to perform oxidation and reduction reactions. The reaction heat can be transferred to the high-pressure gas for expansion, ultimately converting the chemical energy of the fuel into electrical energy. To reduce the energy loss of fuel combustion in conventional liquid natural gas (LNG) power plants, Ishida et al. [8] first proposed a CLC-based gas turbine power generation system, achieving a thermal efficiency of 50.2 %. Liu et al. [9] compared the power generation performance of the CLC and oxy-fuel combustion modes. The results showed that the CLC provided a net power efficiency advantage of 3.93 percentage points, and integrating the supercritical cycle with CLC yielded an additional 0.93 percentage point efficiency gain. Among the various oxy-fuel combustion power cycles, the Allam cycle, which uses

---

* Corresponding authors at: The Turbomachinery Institute, School of Mechanical Engineering, Beijing Institute of Technology, Beijing 100081, China.
E-mail addresses: yangce@bit.edu.cn (C. Yang), hanzhizhang@bit.edu.cn (H. Zhang), buchenwu@ust.hk (B. Wu).

https://doi.org/10.1016/j.applthermaleng.2025.125492
Received 23 August 2024; Received in revised form 25 November 2024; Accepted 7 January 2025

Nomenclature

$\dot{E}$	exergy rate, kW
h	enthalpy, kJ/kg
$\dot{I}$	exergy loss, kW
$\dot{m}$	mass flow rate, kg/s
p	pressure, MPa
Q	heat transfer, kW
s	entropy, kJ/kg/K
T	temperature, °C
$\dot{W}$	power, MW

Greek letters

α	cooling-to- electricity power ratio
η	efficiency, %

Subscripts

el	electrical
ex	exergy
net	net power

Abbreviations

AR	air reactor
AC	air compressor
AT	air turbine
CC	CO_2 compressor
CCP	combined cooling and power
CLC	chemical looping combustion
CLC-BC	CLC-driven Brayton cycle
CT	CO_2 turbine
Eva	evaporator
FR	fuel reactor
GT	gas turbine
HPTV	high-pressure throttle valve
LNG	liquid natural gas
LPTV	low-pressure throttle valve
OC	oxygen carrier
REG	regenerator
Sep	separator

supercritical CO_2 as the working medium, is noted for its efficient energy conversion and CO_2 capture [10], but the cryogenic air separation process is energy-intensive [11]. Saqline et al. [12] and Liu et al. [13] demonstrated that replacing conventional cryogenic air separation with chemical looping air separation increased the net power efficiency of the Allam cycle by 6 and 9.5 percentage points, respectively. As an innovative heat-to-electricity conversion technology, the SCO_2 cycle shows significant potential for application in different thermal energy fields due to its high efficiency and compactness [14–17]. Consequently, the CLC-based SCO_2 (CLC-SCO_2) cycle has emerged as a prominent research topic, with configurations classified into direct [12,13] and indirect [18,19] layouts according to the CO_2 heating method. Khallaghi et al. [18] evaluated the thermoeconomic performances of the oxy-fuel combustion- and CLC-driven SCO_2 cycles. They found that the CLC-SCO_2 cycle offered a 2.7 percentage points advantage in net efficiency and a 1.8 $/MWh benefit in levelized cost of electricity. Wang et al. [19] investigated the performance of the indirect CLC-SCO_2 cycle under atmospheric and pressurized reactor conditions. The results indicated that the pressurized mode improved the system's exergy efficiency by 1.16 percentage points.

Reasonably utilizing the waste heat from the two post-reaction gases in the CLC system can effectively enhance energy efficiency. Du et al. [20] improved the electrical efficiency of the system by 2.78 percentage points by integrating a portion of the waste heat from the post-reaction air into the direct CLC-SCO_2 cycle. Wang et al. [21] and Du et al. [22] developed CLC-driven SCO_2 and organic Rankine combined cycles for energy cascading, achieving power generation efficiencies of 51.79 % and 52.68 %, respectively. Ma et al. [23] diverted all reaction waste heat from the CLC unit into an absorption refrigeration device, resulting in the exergy and power generation efficiencies of the combined system being 46.38 % and 46.74 %, respectively. In power generation-only systems, the exergy input from the fuel exceeds its energy input, leading to a notable difference between exergy and power generation efficiencies. The two efficiencies reported in Ref. [23] are comparable because the additional cooling exergy enhances the exergy efficiency while the absence of excess electrical power limits improvements in power generation efficiency. Given the reduction in power output due to cooling energy production, it is crucial to explore the low-grade waste heat-driven combined cooling and power (CCP) strategies for flexible adjustments in cooling and power generation capacities. While employing a combined cycle (e.g., separate power generation and refrigeration units) can achieve this, it may complicate system design. Therefore, developing a stand-alone cycle for waste heat recovery that can simultaneously perform CCP functions appears to be a more practical approach.

Thermodynamically, common refrigeration effects are achieved under adiabatic conditions through methods such as expansion and throttle. These techniques have led to the development of the self-condensing transcritical CO_2 (tCO_2) cycle, which addresses the challenge of liquefying SCO_2 in dry environments. Pan et al. [24] introduced a self-condensing tCO_2 cycle using an expander to transition the working medium into the two-phase region. They found that the thermal efficiency of the proposed cycle at 34.63 % was lower than that of the SCO_2 reheat cycle at 37.77 %. Building on this, Haq et al. [25] enhanced the thermal efficiency to 39.82 % by modifying the layout. Researchers including Zhu and Cetin [26], Wan et al. [27], and Chen et al. [28] designed self-condensing tCO_2 cycles with different configurations using vortex tubes. They obtained thermal efficiencies of 35.50 %, 38.71 %, and 42.00 %, and exergy efficiencies of 58.21 %, 65.09 %, and 66.10 %, respectively, under baseline conditions. Xia et al. [29] and Guo et al. [30] developed ejector-based self-condensing tCO_2 cycles. They improved the exergoeconomic of the system for both power generation and cogeneration of heat and electricity through layout modifications. Liu et al. [31] established a liquid CO_2 energy storage system based on an ejector condensation cycle and found that the exergy destruction within the ejector condensation cycle decreased significantly with low-pressure tank temperature (i.e., condensation temperature). Despite these advancements, the self-condensing mode that reduces the lowest temperature of CO_2 in the loop does not produce a cooling effect. This is because lower condensing temperatures necessitate lower condensing pressures, which can diminish system efficiency by increasing the power consumption for compression.

In summary, the CLC technology has been shown to facilitate the clean use of carbon-based fuels and can be combined with the SCO_2 cycle for efficient electricity generation. When refrigeration capacity is required, incorporating a CCP unit to recover waste heat from CLC-based systems is essential for flexible adjustment of thermodynamic performance, yet it remains a research gap. Among various waste heat-driven thermodynamic systems, a stand-alone self-condensing tCO_2 cycle is more practical than a combined cycle with complex configurations for fulfilling CCP needs. However, the application of self-condensing tCO_2 cycles for CCP is limited due to the constraints of existing self-condensing methods. For instance, expanders face challenges such as low efficiency, blade corrosion, and high friction losses due to the two-phase state of CO_2 [24,25]. Vortex tubes and ejectors achieve low-temperature self-condensing only at lower liquefaction pressures [26–28], which can significantly augment compression power consumption due to the higher gas-phase composition. Therefore, a two-stage adiabatic throttle driven by different pressure drops is recommended to equip the self-condensing tCO_2 cycle with refrigeration capability. The first-stage throttle valve addresses the reduction of gas-phase composition, while the second-stage throttle valve ensures a certain cooling capacity.

This study presents a two-stage throttle-based self-condensing tCO_2 cycle, which actualizes CCP by recovering low-grade waste heat. This method enables the avoidance of significant reductions in thermodynamic efficiency associated with cold energy production through flexible regulation. Based on this concept, a CLC-based dual-throttle self-condensing tCO_2 cycle system is proposed, aiming to achieve efficient cogeneration of cooling and power through clean utilization of natural gas. A thermodynamic model of the proposed system is developed, followed by exergy flow distribution and parameter analysis to examine component exergy destruction and the effects of key parameters on system performance. A multi-objective optimization is then performed to balance power generation and cooling capacities. The novelties and contributions of this study are as follows:

(1) A dual-throttle approach for the self-condensing of CO_2 is introduced. By adjusting the back pressure of the first-stage throttle valve, the gas–liquid phase composition can be controlled, allowing flexible regulation of both compression power consumption and refrigeration capacity. This self-condensing tCO_2 cycle offers both methodological and theoretical support for the simultaneous conversion of low-grade waste heat into electricity and cooling energy.

(2) A zero-carbon emission combined cooling and power system, integrating a Cu-based CLC unit with a dual-throttle self-condensing tCO_2 cycle, is proposed. Various adjustment methods and optimal design boundary of the system's cooling-to-electricity power ratio are determined.

2. System description

The layout of the proposed cogeneration system is depicted in Fig. 1 (a), featuring a CLC-based Brayton cycle (CLC-BC) upstream and a self-condensing tCO_2 cycle downstream. The CLC equipment converts the chemical energy of the fuel into thermal energy through contactless combustion. Oxygen carriers are integral to the CLC process, with their types directly influencing the CCL performance. Cu-based oxygen carriers are attractive due to their high reactivity with fuels compared to other metal oxides, facilitating complete reactions reaction within the CLC and enabling efficient CO_2 capture [32]. However, the relatively low melting temperature of Cu-based oxygen carriers restricts the reactor's operating temperature to below 900 °C to prevent agglomeration [32]. The use of a support phase can enhance the mechanical strength and thermal stability of the oxygen carrier. Adanez et al. [33] experimentally demonstrated that a $MgAl_2O_4$-based support phase enables Cu-based oxygen carriers to remain sinter-free at an operating temperature of 950 °C. Consequently, this study employs a mass ratio of 6:4 for $MgAl_2O_4$-supported CuO/Cu to transport the oxygen element. The chemical reactions occurring in the two reactors are represented by Eqs. (1) and (2), respectively, with an excess of CuO and O_2 required to ensure thorough reactions.

$$\mathrm{FR}: 4\mathrm{CuO} + \mathrm{CH_4} \rightarrow 4\mathrm{Cu} + \mathrm{CO_2} + 2\mathrm{H_2O}\ \Delta H = -217.1\mathrm{kJ/kmol} \tag{1}$$

$$\mathrm{AR}: 2\mathrm{Cu} + \mathrm{O_2} \rightarrow 2\mathrm{CuO}\ \Delta H = -314.6\mathrm{kJ/kmol} \tag{2}$$

The upstream CLC-BC is powered by a fuel reactor (FR) and an air reactor (AR), generating electricity through expansion in a gas turbine (GT) and an air turbine (AT). In the FR, the oxygen carrier is reduced by natural gas transported by the fuel compressor (FC), and its operating temperature is controlled by the recirculated CO_2 with a cooling effect.

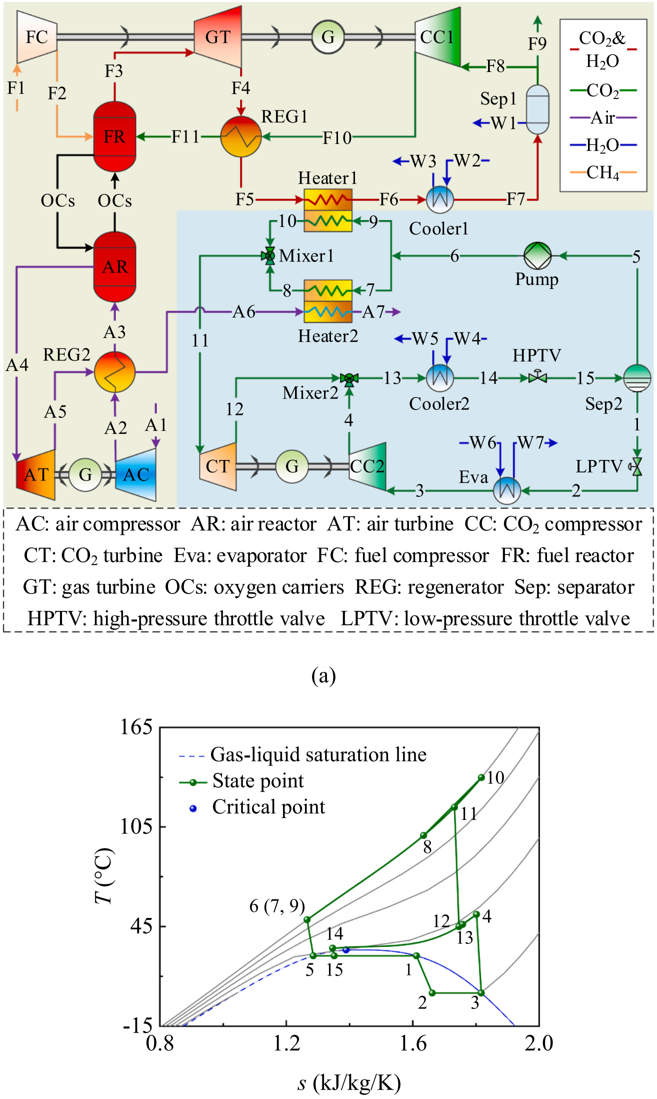

(a)

(b)

Fig. 1. Layout (a) and downstream *T-s* diagram (b) of the CLC-based cogeneration system.

Following expansion in the GT, the post-reaction gas mixture passes through the regenerator1 (REG1), heater1, and cooler1, releasing heat at each stage. The cooled gas mixture then enters the separator1 (Sep1) for dehydration, where a portion of the dried CO_2 is captured before recirculation. The recirculated CO_2 is first pressurized by the CO_2 compressor1 (CC1) and then heated by the REG1 before entering the FR. In the AR, the oxygen carrier is oxidized by air, which is first compressed by an air compressor (AC) and then heated by the REG2. After the nitrogen-rich air expands in the AT, it dissipates heat sequentially in the REG2 and heater2 before being discharged into the atmosphere.

The downstream dual-throttle self-condensing tCO_2 cycle achieves CCP by recovering waste heat from the upstream process through two heaters, as depicted in its temperature-entropy (*T-s*) diagram in Fig. 1 (b). The CO_2 exiting the cooler2 undergoes adiabatic expansion from a supercritical state to a two-phase state with a low vapor fraction in the high-pressure throttle valve (HPTV). The two-phase CO_2 is then separated into saturated liquid and saturated gas in the separator2 (Sep2). The saturated liquid CO_2 is pressurized by a pump before flowing into the two parallel heaters for heat absorption and subsequently entering the CO_2 turbine (CT) for expansion. The saturated gaseous CO_2

undergoes adiabatic expansion to a low-temperature two-phase state in the low-pressure throttle valve (LPTV). The low-temperature two-phase CO_2 absorbs heat in the evaporator (Eva) to reach a saturated gaseous state before entering the CC2 for compression. The two streams of SCO_2 flowing out of CT and CC2 are mixed and then re-enter the cooler2. Additionally, when the saturated gaseous stream at the Sep2 outlet bypasses the LPTV and Eva and flows directly into the CC2, the dual-throttle self-condensing transitions into a single-throttle self-condensing.

3. System modeling

3.1. Methodology and assumptions

In this study, the thermodynamic processes of the proposed system are simulated using two platforms: ASPEN PLUS and MATLAB. The Cu-based CLC process is modeled in ASPEN PLUS by employing two RGibbs-type reactors, with the equilibrium state determined by minimizing Gibbs's free energy. The thermophysical properties of the substances are obtained through the Peng-Robinson equation of state in ASPEN PLUS and NIST REFPROP in MATLAB [34]. The base design parameters for the cogeneration system are summarized in Table 1, with the pinch-point temperature difference set at 10 °C for heaters and regenerators and 5 °C for coolers and evaporators. Furthermore, the following assumptions are made to simplify the simulation and analysis processes of the system:

(1) The system maintains a steady-state operation without leakage of the working medium.

(2) The composition of natural gas is 100 % CH_4, and the composition of air is 21 % O_2 and 79 % N_2.

(3) Ignore the pressure drop and heat dissipation for all components.

(4) The temperatures of the substances at the reactor outlet are equal.

(5) The two reactors are treated as a whole during exergy analysis.

3.2. Component model

The system model is constructed by integrating the component models based on the principles of energy and mass conservation. Beyond the two reactors, the thermodynamic models for the turbomachinery, throttle valves, and heat exchangers are essential. The compression components and turbines are modeled as Eqs. (3) and (4), respectively, with their power output shown in Eq. (5).

Table 1
Base design parameters of the system.

Items	Values
Ambient temperature, T_0 (°C)	25.00
Ambient pressure, p_0 (MPa)	0.10
Generator efficiency, η_{gen} (%)	98.50
Pinch-point temperature difference of HEX, ΔT_{pp} (K) [22]	10.00 and 5.00
CLC-BC unit	
CH_4 flow rate, $\dot{m}_{F1}$ (kg/s) [22]	1.00
Outlet temperature at fuel reactor, T_{F3} (°C) [18]	900.00
Outlet temperature at air reactor, T_{A4} (°C) [13]	950.00
Reactor operating pressure, $p_{F2/A3}$ (MPa)	0.20
Mass ratio of $MgAl_2O_4$ to CuO, [22]	1.50
Excess coefficient of CuO, [13]	1.40
Compressor efficiency, η_{comp} (%)	90.00
Turbine efficiency, η_{turb} (%)	92.00
Water temperature at cooler1 outlet, T_{W3} (°C)	30.00
Self-condensing tCO$_2$ unit	
Pump inlet pressure, p_5 (MPa)[26]	6.80
Pump outlet pressure, p_6 (MPa)	15.00
CO_2 turbine outlet pressure, p_4 (MPa)	7.70
Pump efficiency, η_{pump} (%) [25]	65.00
CO_2 Compressor efficiency, η_{comp} (%) [25]	80.00
CO_2 turbine efficiency, η_{turb} (%) [25]	88.00
HPTV inlet temperature, T_{14} (°C)	32.00
Evaporation temperature, T_2 (°C)	5.00
CO_2 Compressor inlet temperature, T_3 (°C)	10.00

$$\eta_{comp} = \frac{h_{out,s} - h_{in}}{h_{out} - h_{in}} \tag{3}$$

$$\eta_{turb} = \frac{h_{in} - h_{out}}{h_{in} - h_{out,s}} \tag{4}$$

$$W_{comp/turb} = m \times (h_{out/in} - h_{in/out}) \tag{5}$$

where h_{in} and h_{out} represent the inlet and outlet enthalpies of the component, respectively. The subscript $_s$ is the isentropic condition.

The outlet pressure of the HTPV and the outlet temperature of the LPTV are known, so their outlet states after adiabatic expansion can be determined by Eqs. (6) and (7), respectively.

$$T_{out} = f(p_{out}, h(T_{in}, p_{in})) \tag{6}$$

$$p_{out} = f(T_{out}, h(T_{in}, p_{in})) \tag{7}$$

The heat exchangers, designed with a counter-flow layout, are modeled by setting the pinch-point temperature difference (ΔT_{pp}). Due to the drastic physical changes of CO_2, particularly near its supercritical point (30.97 °C, 7.38 MPa), the pinch point may occur inside the heat exchanger. Therefore, the pinch point is identified using a discrete approach described in Eq. (8).

$$Q_n = m_c \times (h_{c,n+1} - h_{c,n}) = m_h \times (h_{h,n} - h_{h,n+1}) \tag{8}$$

where Q is the heat transfer capacity. The subscripts $_h$ and $_c$ denote the hot and cold fluids, respectively. n is the discrete number.

3.3. Exergy analysis

Exergy analysis, a well-established thermodynamic tool, is employed to evaluate the energy utilization of the system by providing insights into component-level exergy flow distribution. Excluding kinetic exergy and potential exergy, the exergy ($\dot{E}$) of the working medium is characterized as physical exergy ($\dot{E}_{\text{ph}}$) and chemical exergy ($\dot{E}_{\text{ch}}$), i.e. Eq. (9).

$$\dot{E} = \dot{E}_{ch} + \dot{E}_{ph} \tag{9}$$

By treating the two reactors as a single entity, the need to consider the exergy of the solid phase during exergy analysis is eliminated. Thus, the physical exergy of fluids is represented by Eq. (10), and the chemical exergy is only considered in processes involving CH_4, which has a chemical exergy of 51.90 MJ/kg [35].

$$E_{ph} = m \times [(h - h_0) - T_0(s - s_0)] \tag{10}$$

where the subscript $_0$ is the ambient condition. *LHV* is the low heating value of CH_4, 50 MJ/kg.

The exergy balance equation for the k^{th} component is expressed as Eq. (11).

$$\dot{E}_{in,k} + \dot{W}_{in,k} = \dot{E}_{out,k} + \dot{I}_k \tag{11}$$

where $\dot{E}_{in,k}$+$\dot{W}_{in,k}$, $\dot{E}_{out,k}$+$\dot{W}_{out,k}$, and I_k denote the exergy fuel (i.e. the sum of input exergy and input work), exergy production (i.e. the sum of output exergy and output work), exergy destruction, respectively. Accordingly, the detailed exergy balance equations for each component are shown in Table 2.

3.4. Performance index

The system's thermodynamic performance is evaluated through electrical efficiency (η_{el}) and exergy efficiency (η_{ex}), expressed as Eqs. (12) and (13), respectively. Additionally, the system's cooling capacity is characterized by defining the cooling-to-electricity power ratio (α), as

Table 2
Exergy balance equations for each component.

Components	$\dot{E}_{in}+\dot{W}_{in}$	$\dot{E}_{out}+\dot{W}_{out}$	$\dot{I}$
FC	$\dot{W}_{FC}$	$\dot{E}_{F2}-\dot{E}_{F1}$	$\dot{W}_{FC}-(\dot{E}_{F2}-\dot{E}_{F1})$
FR&AR	$\dot{E}_{F2}+\dot{E}_{F11}+\dot{E}_{A3}$	$\dot{E}_{F3}+\dot{E}_{A4}$	$\dot{E}_{F2}+\dot{E}_{F11}+\dot{E}_{A3}-(\dot{E}_{F3}+\dot{E}_{A4})$
GT	$\dot{E}_{F3}-\dot{E}_{F4}$	$\dot{W}_{GT}$	$\dot{E}_{F3}-\dot{E}_{F4}-\dot{W}_{GT}$
Cooler1	$\dot{E}_{F6}-\dot{E}_{F7}$	$\dot{E}_{W3}-\dot{E}_{W2}$	$\dot{E}_{F6}-\dot{E}_{F7}-(\dot{E}_{W3}-\dot{E}_{W2})$
REG1	$\dot{E}_{F4}-\dot{E}_{F5}$	$\dot{E}_{F11}-\dot{E}_{F10}$	$\dot{E}_{F4}-\dot{E}_{F5}-(\dot{E}_{F11}-\dot{E}_{F10})$
Sep1	$\dot{E}_{F7}$	$\dot{E}_{F8}+\dot{E}_{F9}+\dot{E}_{W1}$	$\dot{E}_{F7}-(\dot{E}_{F8}+\dot{E}_{F9}+\dot{E}_{W1})$
CC1	$\dot{W}_{CC1}$	$\dot{E}_{F10}-\dot{E}_{F8}$	$\dot{W}_{CC1}-(\dot{E}_{F10}-\dot{E}_{F8})$
AT	$\dot{E}_{A4}-\dot{E}_{A5}$	$\dot{W}_{AT}$	$\dot{E}_{A4}-\dot{E}_{A5}-\dot{W}_{AT}$
REG2	$\dot{E}_{A5}-\dot{E}_{A6}$	$\dot{E}_{A3}-\dot{E}_{A2}$	$\dot{E}_{A5}-\dot{E}_{A6}-(\dot{E}_{A3}-\dot{E}_{A2})$
AC	$\dot{W}_{AC}$	$\dot{E}_{A2}-\dot{E}_{A1}$	$\dot{W}_{AC}-(\dot{E}_{A2}-\dot{E}_{A1})$
HE1	$\dot{E}_{F5}-\dot{E}_{F6}$	$\dot{E}_{10}-\dot{E}_{9}$	$\dot{E}_{F5}-\dot{E}_{F6}-(\dot{E}_{10}-\dot{E}_{9})$
HE2	$\dot{E}_{A6}-\dot{E}_{A7}$	$\dot{E}_{8}-\dot{E}_{7}$	$\dot{E}_{A6}-\dot{E}_{A7}-(\dot{E}_{8}-\dot{E}_{7})$
Mixer1	$\dot{E}_{10}+\dot{E}_{8}$	$\dot{E}_{11}$	$\dot{E}_{10}+\dot{E}_{8}-\dot{E}_{11}$
CT	$\dot{E}_{11}-\dot{E}_{12}$	$\dot{W}_{CT}$	$\dot{E}_{11}-\dot{E}_{12}-\dot{W}_{CT}$
CC2	$\dot{W}_{CC2}$	$\dot{E}_{4}-\dot{E}_{3}$	$\dot{W}_{CC2}-(\dot{E}_{4}-\dot{E}_{3})$
Mixer2	$\dot{E}_{12}+\dot{E}_{4}$	$\dot{E}_{13}$	$\dot{E}_{12}+\dot{E}_{4}-\dot{E}_{13}$
Cooler2	$\dot{E}_{13}-\dot{E}_{14}$	$\dot{E}_{W5}-\dot{E}_{W4}$	$\dot{E}_{13}-\dot{E}_{14}-(\dot{E}_{W5}-\dot{E}_{W4})$
HPTV	$\dot{E}_{14}$	$\dot{E}_{15}$	$\dot{E}_{14}-\dot{E}_{15}$
Sep2	$\dot{E}_{15}$	$\dot{E}_{1}+\dot{E}_{5}$	$\dot{E}_{15}-(\dot{E}_{1}+\dot{E}_{5})$
Pump	$\dot{W}_{CP}$	$\dot{E}_{6}-\dot{E}_{5}$	$\dot{W}_{CP}-(\dot{E}_{6}-\dot{E}_{5})$
LPTV	$\dot{E}_{1}$	$\dot{E}_{2}$	$\dot{E}_{1}-\dot{E}_{2}$
Evaporator	$\dot{E}_{2}-\dot{E}_{3}$	$\dot{E}_{W7}-\dot{E}_{W6}$	$\dot{E}_{2}-\dot{E}_{3}-(\dot{E}_{W7}-\dot{E}_{W6})$

given in Eq. (14).

$$\eta_{el} = \frac{W_{net}}{m_{CH_4} \times LHV} \tag{12}$$

$$\eta_{ex} = \frac{W_{net} + (E_{W7} - E_{W6})}{E_{F1}} \tag{13}$$

$$\alpha = \frac{W_{Eva}}{W_{net}} \tag{14}$$

where $W_{\rm net}$ represents the net power generation, as shown in Eq. (15).

$$W_{net} = (W_{GT} + W_{AT} + W_{CT}) \times \eta_{gen} - W_{FC} - W_{CC1} - W_{CC2} - W_{AC} - W_{Pump} \tag{15}$$

3.5. Model verification

Given that the proposed system primarily consists of CLC and self-condensing tCO_2 units, this section validates the modeling approach for these two cycles. The validation results for the CLC unit obtained based on Ref. [36] are detailed in Table 3. A maximum relative deviation of 1.60 % confirms the reliability of using ASPEN PLUS for CLC modeling. Additionally, Table 4 presents comparative results for the nodal thermophysical properties of the self-condensing tCO_2 cycle based on Ref. [25]. A maximum relative deviation of less than 0.1 % underscores the high accuracy of the thermodynamic modeling approach.

Table 3
Validation results for the CLC unit.

Reactors	Parameters		Ref. [36]	Present	Dev (%)
Fuel reactor	T (°C)		723.00	721.11	0.26
	Mole flow (kmol/s)		2.999	2.998	0.03
	Mole fraction (–)	CO_2	0.3333	0.3334	0.02
		H_2O	0.6665	0.6664	0.01
Stream reactor	T (°C)		727.00	724.64	0.46
	Mole flow (kmol/s)		6.55	6.55	0
	Mole fraction (–)	H_2O	0.5938	0.5929	0.15
		H_2	0.4062	0.4071	0.22
Air reactor	T (°C)		880.00	865.89	1.60
	Mole flow (kmol/s)		2.5380	2.5483	0.41

Table 4
Validation results for the self-condensing tCO_2 cycle.

Nodes	T (°C)			h (kJ/kg)		
	Ref. [25]	Present	Dev (%)	Ref. [25]	Present	Dev (%)
01	550.00	550.00	0	1031.8	1031.8	0
02	421.25	421.25	0	891.70	891.70	0
03	148.76	148.76	0	579.20	579.20	−0.01
04	63.25	63.24	−0.02	460.70	460.60	−0.01
05	35.00	35.00	0	318.60	318.50	−0.02
06	18.88	18.88	0	314.20	314.20	0.01
07	18.88	18.88	0	410.10	410.10	0.01
08	18.88	18.88	0	252.10	252.10	0.01
09	138.76	138.76	0	483.20	483.10	−0.01
10	47.30	47.31	0.01	287.90	287.90	0
11	360.98	360.98	0	795.70	795.70	0

4. Results and discussion

The cogeneration performance of the proposed CLC-based self-condensing tCO_2 cycle is evaluated through performance comparisons, parametric analysis, and multi-objective optimization. The detailed findings are presented below.

4.1. Base design-based system performance

The impact of the dual-throttle mode on system performance is examined by comparing it with the single-throttle mode under base design conditions. As shown in Table 5, the net power generation in dual-throttle mode is 627.98 kW lower than that in single-throttle mode. This reduction is attributed to the increased compression power consumption due to the larger pressure ratio of the CO_2 compressor2 in dual-throttle mode. The presence of the low-pressure throttle valve and evaporator allows the dual-throttle mode to produce a cooling capacity of 1132.46 kW. As a result, the electrical and exergy efficiencies of the dual-throttle mode with CCP effect are reduced by 1.25 and 1.15 percentage points, respectively, compared to the power generation-solely single-throttle mode. Nevertheless, the electrical efficiency of 52.02 % and exergy efficiency of 50.17 % under dual-throttle configuration underscore the necessity of further exploring the proposed system. The thermophysical parameters of the nodes within the proposed system under base design conditions are detailed in Table 6. With a CH_4 flow rate of 1 kg/s, the system requires a CO_2 flow rate of 97.33 kg/s and an air flow rate of 137.53 kg/s to maintain operating temperatures of 900 °C in the fuel reactor and 950 °C in the air reactor. The waste heat-driven self-condensing tCO_2 cycle engenders a CO_2 flow of 84.00 kg/s for power generation and 21.41 kg/s for refrigeration, corresponding to a dryness value of 0.20 at the separator2 inlet. Consequently, the upstream cycle consumes a total compression work of 14652.51 kW and

Table 5
Base design performance of the system in both modes.

Items	Single-throttle mode	Dual-throttle mode
Energy input, (kW)	50000.00	
Exergy input, (kW)	51900.00	
$\dot{W}_{FC}$, (kW)	126.11	
$\dot{W}_{CC1}$, (kW)	4645.85	
$\dot{W}_{GT}$, (kW)	13916.96	
$\dot{W}_{AC}$, (kW)	9880.55	
$\dot{W}_{AT}$, (kW)	27294.11	
$\dot{W}_{pump}$, (kW)	1487.02	
$\dot{W}_{CT}$, (kW)	2297.09	
$\dot{W}_{CC2}$, (kW)	83.72	707.96
$\dot{W}_{net}$, (kW)	26636.03	26008.05
$\dot{W}_{cooling}$, (kW)	0	1132.46
$\dot{E}_{cooling}$, (kW)	0	29.50
η_{el}, (%)	53.27	52.02
η_{ex}, (%)	51.32	50.17
α	0	0.04

Table 6
Nodal thermophysical properties of the proposed system under base design conditions.

Nodes	Working fluid	T (°C)	p (MPa)	$\dot{m}$ (kg/s)	$\dot{E}$ (kW)
F1	CH_4	25.00	0.10	1.00	53000.00
F2	CH_4	80.08	0.20	1.00	52015.38
F3	CO_2/water	900.00	0.20	102.33	60486.67
F4	CO_2/water	794.40	0.10	102.33	46230.26
F5	CO_2/water	151.95	0.10	102.33	2086.14
F6	CO_2/water	56.65	0.10	102.33	177.55
F7	CO_2/water	30.00	0.10	102.33	13.76
F8	CO_2	30.00	0.10	97.33	3.45
F9	CO_2	30.00	0.10	2.75	0.10
F10	CO_2	83.42	0.20	97.33	4141.11
F11	CO_2	784.40	0.20	97.33	45962.86
A1	Air	25.00	0.10	137.53	0
A2	Air	95.73	0.20	137.53	9074.24
A3	Air	750.14	0.20	137.53	61803.36
A4	Nitrogen-rich air	950.00	0.20	133.53	83130.63
A5	Nitrogen-rich air	776.43	0.10	133.53	55157.35
A6	Nitrogen-rich air	105.73	0.10	133.53	1266.75
A7	Nitrogen-rich air	56.71	0.10	133.53	226.95
1	CO_2	27.41	6.80	21.41	4583.16
2	CO_2	5.00	3.97	21.41	4264.85
3	CO_2	10.00	3.97	21.41	4185.36
4	CO_2	64.53	7.70	21.41	4767.60
5	CO_2	27.41	6.80	84.00	17914.45
6	CO_2	46.65	15.00	84.00	18914.60
7	CO_2	46.65	15.00	44.12	9933.44
8	CO_2	95.73	15.00	44.12	10782.37
9	CO_2	46.65	15.00	39.89	8981.16
10	CO_2	141.95	15.00	39.89	10520.80
11	CO_2	115.43	15.00	84.00	21225.31
12	CO_2	61.14	7.70	84.00	18647.98
13	CO_2	61.81	7.70	105.41	23415.12
14	CO_2	32.00	7.70	105.41	22660.64
15	CO_2	27.41	6.80	105.41	22497.60
W1	Water	30.00	0.10	2.25	0.39
W2	Water	25.00	0.10	167.11	0
W3	Water	30.00	0.10	167.11	28.96
W4	Water	25.00	0.10	430.57	0
W5	Water	34.33	0.10	430.57	257.55
W6	Water	25.00	0.10	18.03	0
W7	Water	10.00	0.10	18.03	29.50

produces a total expansion work of 41211.07 kW, as illustrated in Table 5. The downstream cycle exhibits a compression power consumption of 2194.98 kW and an expansion power of 2297.09 kW.

Fig. 2 depicts the exergy flow distribution within the proposed system under base design conditions. The exergy distribution of each component is listed in Table 7. The total exergy destruction of the system is approximately 25862.45 kW, with 23575.99 kW attributed to the upstream cycle and 2286.46 kW to the downstream cycle. In the upstream cycle, the highest exergy destruction is 16134.80 kW in the two reactors, resulting from irreversible chemical reactions. This is followed by 2322.38 kW in the regenerator1 and 1161.48 kW in the regenerator2. In the downstream cycle, the exergy destruction of the cooler2, CO_2 pump, and low-pressure throttle valve is relatively high, with values of 496.94 kW, 486.86 kW, and 318.30 kW, respectively. The exergy flow for power generation and refrigeration is distributed among four components. The exergy fuel input to the gas turbine is 14256.42 kW, with 97.62 % converted into output work and 2.38 % lost as irreversibility. The exergy fuel of the air turbine is 27973.27 kW, consisting of exergy production of 97.57 % and exergy destruction of 2.43 %. The CO_2 turbine operates with an exergy fuel of 2577.33 kW, where 89.13 % is utilized for output and 10.87 % is destroyed. The evaporator has an exergy input of 79.49 kW, with 37.11 % used for refrigeration and the remainder lost.

The ratio of exergy production to exergy fuel of a component represents its exergy efficiency. Accordingly, the exergy efficiencies of the cooler1, cooler2, and evaporator are relatively low, at 17.68 %, 34.14 %, and 37.11 %, respectively. This diminished performance in these heat exchangers is primarily due to substantial terminal temperature differences, despite a small pinch-point temperature difference. The abrupt changes in physical properties during the phase transition and near the critical point of the working fluid contribute to these inefficiencies. To analyze these effects, the heat transfer processes of cooler1, cooler2, and the evaporator were examined and their T-Q diagrams at 1000 discrete numbers are shown in Fig. 3. Fig. 3(a) illustrates the cooling process of the binary mixture in the cooler1, where the mixture transitions from a gaseous state to a two-phase state. The saturated vapor pressure varies and temperature decreases gradually during condensation, influenced by the mixture composition. The water temperature rises as the mixture temperature falls, with minimum and maximum temperature differences of 5 °C and 26.65 °C occurring at the cold and hot ends, respectively. The cooling process of sCO_2 in the cooler2 is depicted in Fig. 3(b). In the constant-pressure region near the critical point, the heat capacity of CO_2 sharply decreases and then increases as the temperature drops, leading to a rapid initial cooling followed by slower cooling. The pinch point occurs at a heat transfer capacity of 9726.22 kW, with the maximum temperature difference of 27.48 °C found at the hot end. Unlike the two coolers, the maximum temperature difference of the evaporator is inside it rather than at the terminal, as shown in Fig. 3(c). This is due to the lower heat capacity of the gaseous state compared to the two-phase state. The maximum temperature difference of 17.22 °C is observed at the location of the saturated gaseous state of CO_2, with a minimum temperature difference of 5 °C at the cold end. The heat absorption in the two-phase region is crucial for outputting cold energy by producing chilled water.

4.2. *Parameter analysis*

A comprehensive parameter analysis is conducted to investigate the impact of key design parameters on the performance of the proposed system. The parameters discussed cover upstream reactor pressure (p_{reactor}), fuel reactor temperature (T_{FR}), and air reactor temperature (T_{AR}), as well as downstream pump outlet pressure (p_6) and CO_2 turbine outlet pressure (p_{12}). When analyzing a certain parameter, all other parameters are held at their base design values.

4.2.1. *Reactor pressure*

Fig. 4 exhibits that the effect of increasing p_{reactor} from 0.2 MPa to 0.4 MPa on system performance. As p_{reactor} increases, both the upstream compression and expansion ratios are augmented. This rise in expansion ratios lowers the outlet temperatures of the gas and air turbines, which serve as the heat sources for the two regenerators. Consequently, the temperatures of air and CO_2 (T_{A3} and $T_{\text{ F11}}$) entering their respective reactors decrease, as shown in Fig. 4(a). To maintain constant operating temperatures in both reactors, the air and recirculated CO_2 flow rates ($\dot{m}_{\text{ A3}}$ and $\dot{m}_{\text{F11}}$) decrease by 59.42 kg/s and 44.24 kg/s, respectively. Despite the reduction in upstream flow rates, the increase in expansion and compression ratios leads to higher expansion and compression work, as detailed in Fig. 4(b). Initially, the increase in expansion work outpaces the rise in compression work, causing both electrical and exergy efficiencies to peak at 52.35 % and 50.49 %, respectively, at 0.24 MPa, before declining as p_{reactor} continues to rise, as exemplified in Fig. 4 (c). The reduced hot-side flow rates and temperatures in both heaters lead to a decrease in the downstream CO_2 flow rate, causing the evaporator power to drop by 0.25 MW and the cooling-to-electricity power ratio to decrease from 0.044 to 0.034. The small cooling-to-electricity power ratio explains the concurrent variations observed in electrical and exergy efficiencies.

4.2.2. *Fuel reactor operating temperature*

Fig. 5 illustrates the impact of raising T_{FR} from 800 °C to 900 °C on system performance. Since T_{FR} equals the outlet temperature of the fuel reactor products, this increase leads to higher outlet temperature for the gas turbine and higher T_{F11}, as shown in Fig. 5(a). The elevated T_{F11}

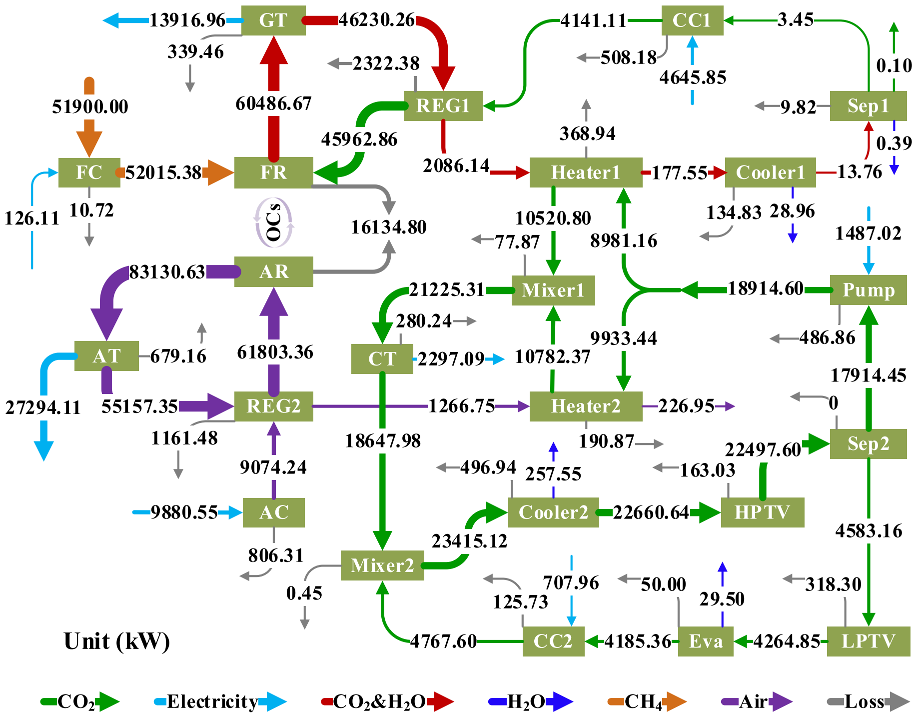

Fig. 2. Exergy flow distribution of the system.

Table 7
Exergy input, exergy output, and irreversibility for each component.

Components	$\dot{E}_{in}+\dot{W}_{in}$ (kW)	$\dot{E}_{out}+\dot{W}_{out}$ (kW)	$\dot{I}$ (kW)
FC	126.11	115.38	10.72
FR&AR	159781.60	143646.80	16134.80
GT	14256.42	13916.96	339.46
Cooler1	163.79	28.96	134.83
REG1	44144.12	41821.74	2322.38
Sep1	13.76	3.94	9.82
CC1	4645.85	4137.67	508.18
AT	27973.27	27294.11	679.16
REG2	53890.61	52729.12	1161.48
AC	9880.55	9074.24	806.31
HE1	1908.58	1539.64	368.94
HE2	1039.80	848.93	190.87
Mixer1	21303.17	21225.31	77.87
CT	2577.33	2297.09	280.24
CC2	707.96	582.24	125.73
Mixer2	23415.58	23415.12	0.45
Cooler2	754.49	257.55	496.94
HPTV	22660.64	22497.60	163.03
Sep2	22497.60	22497.60	0
Pump	1487.02	1000.16	486.86
LPTV	4583.16	4264.85	318.30
Evaporator	79.49	29.50	50.00

necessitates a reduction in the recirculated CO_2 flow rate by 65.29 kg/s to prevent excessive fuel reactor temperatures. Concurrently, the rise in the temperature of the oxygen carriers leaving the fuel reactor requires an increase in the air flow rate into the air reactor by 38.36 kg/s to maintain a constant operating temperature. These changes in upstream flow rates result in decreased power output from the gas turbine and CO_2 compressor1, while the power of the air compressor and air turbine increases, as displayed in Fig. 5(b). Notably, the significant increase in air turbine power enhances the system's net electrical output. Consequently, the electrical and exergy efficiencies of the system improve linearly by 3.10 and 2.98 percentage points, respectively, with the increase in T_{FR}, as shown in Fig. 5(c). However, as the reduction in recirculated CO_2 flow rate outweighs the increase in air flow rate, downstream heat recovery diminishes, leading to a reduction of 0.06 MW and 0.005 in the evaporator power and cooling-to-electricity power ratio.

4.2.3. *Air reactor operating temperature*

Fig. 6 plots the effect of raising T_{AR} from 850 °C to 950 °C on system performance. Since T_{AR} equals the outlet temperature of the air reactor products, the outlet temperature of the air turbine and T_{A3} rise accordingly, as shown in Fig. 6(a). The increase in T_{A3} leads to a reduction in air flow rate by 57.80 kg/s to avoid excessive air reactor temperature. Meanwhile, the elevated temperature of the oxygen carriers leaving the air reactor causes an increase in the recirculated CO_2 flow rate into the fuel reactor by 52.31 kg/s to maintain a constant fuel reactor temperature, given the near-constant T_{F11}. These changes in upstream flow rates increase the power of the gas turbine and CO_2 compressor1 but reduce the power of the air turbine and air compressor, as presented in Fig. 6(b). The overall system experiences a reduction in both compression and expansion work with the rise in T_{AR}, primarily due to the dominant changes in the air-related components. As the reduction in compression work initially exceeds and then falls below the reduction in expansion work, the electrical and exergy efficiencies of the system first increase and then decrease, reaching their peak values of 52.15 % and 50.29 %, respectively, at approximately 910 °C. Additionally, since the decrease in air flow rate surpasses the increase in recirculated CO_2 flow rate, the downstream heat recovery diminishes, resulting in a reduction of 0.04 MW and 0.002 in the evaporator power and cooling-to-electricity power ratio.

4.2.4. *Pump outlet pressure*

Fig. 7 illustrates the impact of increasing p_6 from 10 MPa to 20 MPa on system performance. The change in p_6 affects the system performance exclusively by altering the downstream parameters. As p_6 increases, the pump outlet temperature rises from 35.96 °C to 55.81 °C, leading to a 16.93 kg/s increase in the CO_2 flow rate for power generation by reducing the cold-side enthalpy difference in the two heaters, as depicted in Fig. 7(a). Simultaneously, the CO_2 flow rate for refrigeration augments by4.32 kg/s due to the unchanged vapor composition at the

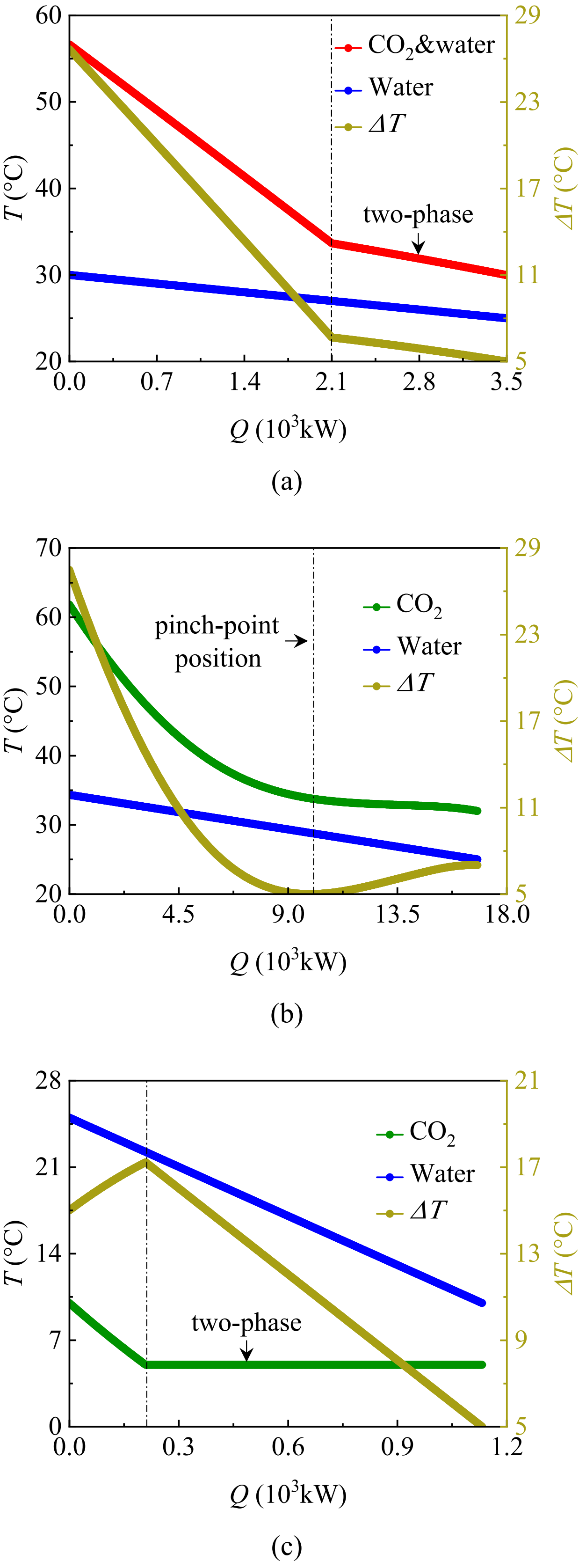

Fig. 3. *T*-*Q* diagrams of the cooler1 (a), cooler2 (b), and evaporator (c).

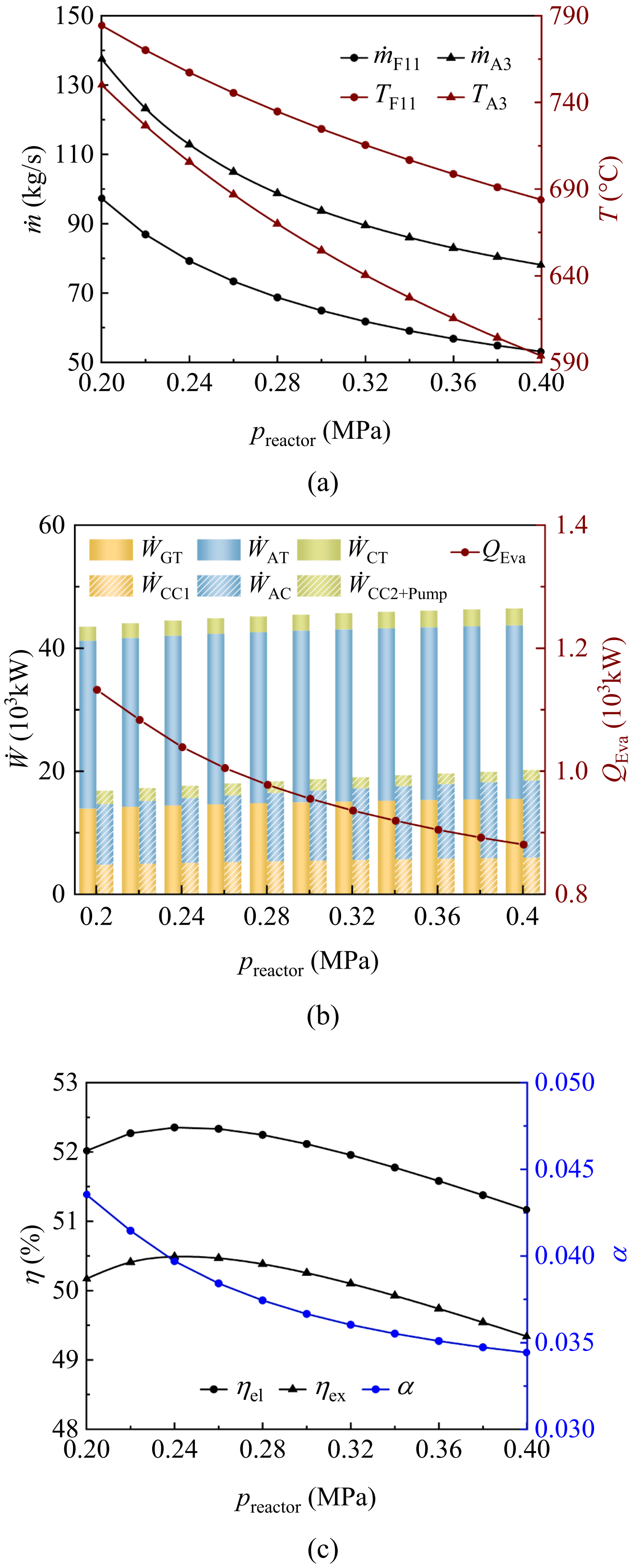

Fig. 4. Influence of reactor pressure on system performance.

separator2 inlet. As a result, the downstream expansion work, compression work, and refrigeration capacity all increase with the rise in p_6, as shown in Fig. 7(b). Since the increment in expansion work is initially larger and then smaller than that in compression work, the

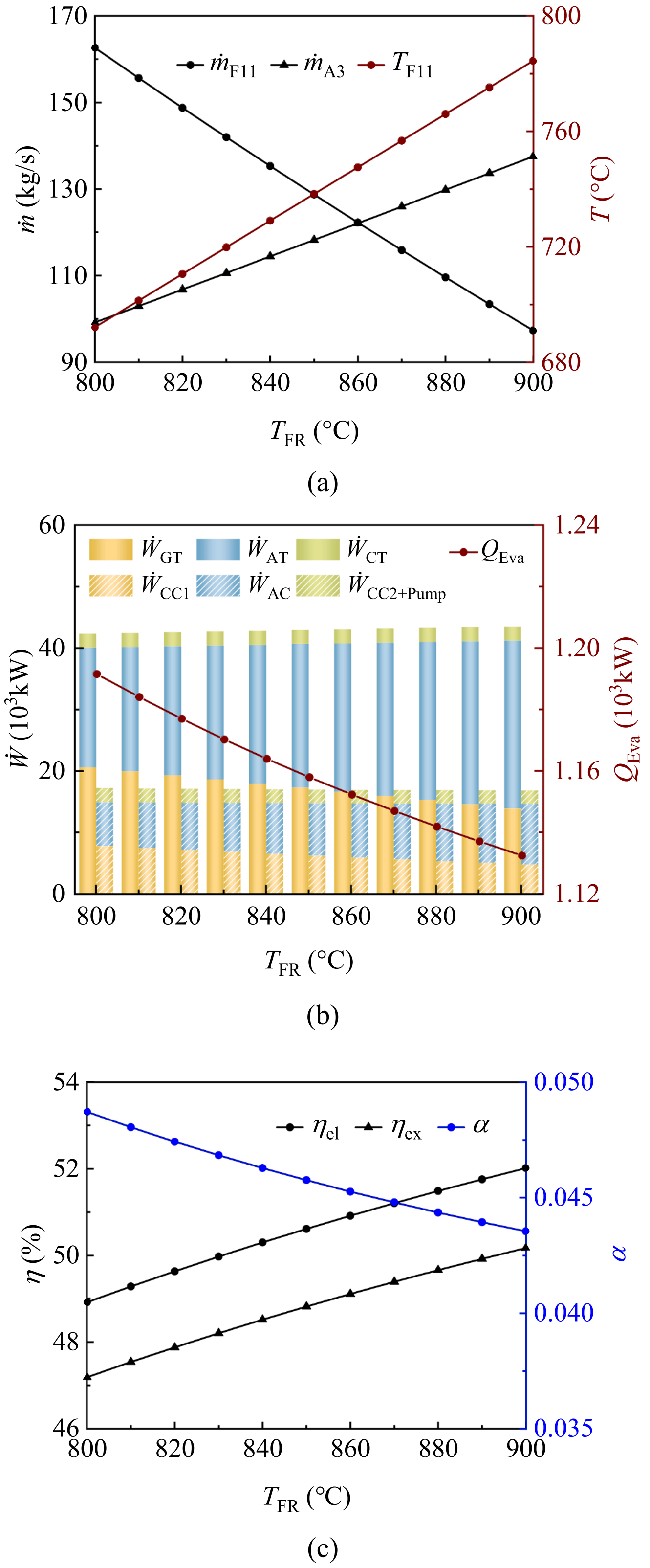

Fig. 5. Influence of fuel reactor temperature on system performance.

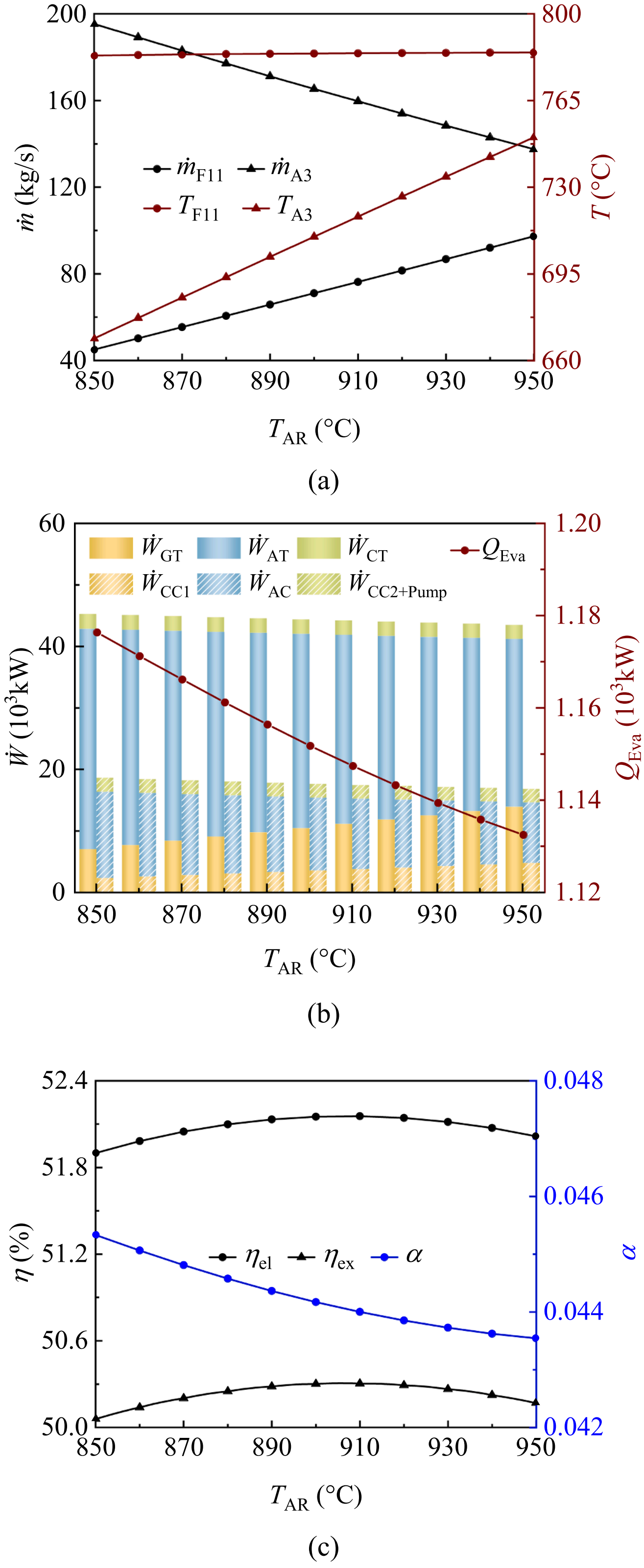

Fig. 6. Influence of air reactor temperature on system performance.

electrical and exergy efficiencies of the system increase and then decrease, peaking at 52.05 % and 50.21 % around 14.00 MPa, respectively. Additionally, the cooling-to-electricity power ratio rises by 0.01, corresponding to a 0.23 MW increase in evaporator power.

4.2.5. CO_2 turbine outlet pressure

Fig. 8 elucidates the effect of increasing p_{12} from 7.7 MPa to 8.7 MPa on system performance. The variation in p_{12} not only alters the power output of downstream turbomachinery but also impacts the vapor–liquid phase composition. As shown in Fig. 8(a), an increase in p_{12}

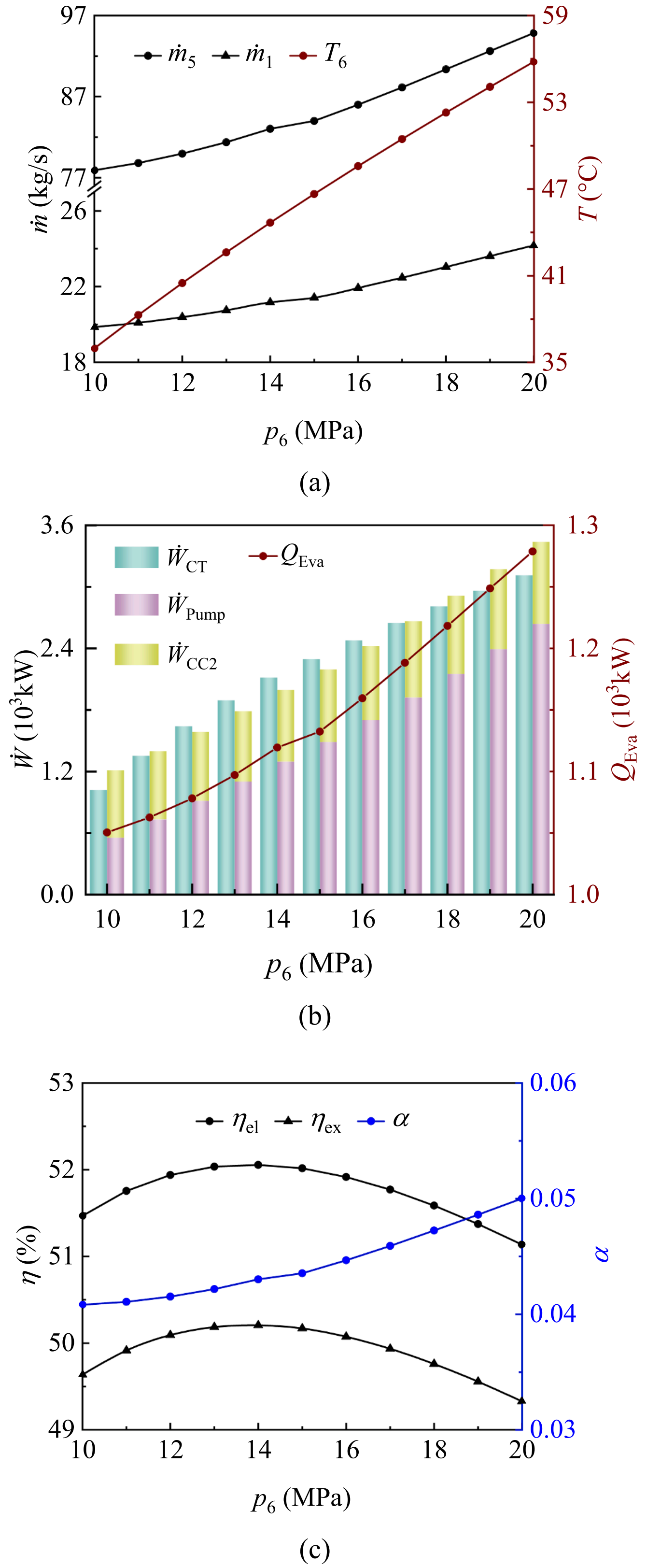

Fig. 7. Influence of pump outlet pressure on system performance.

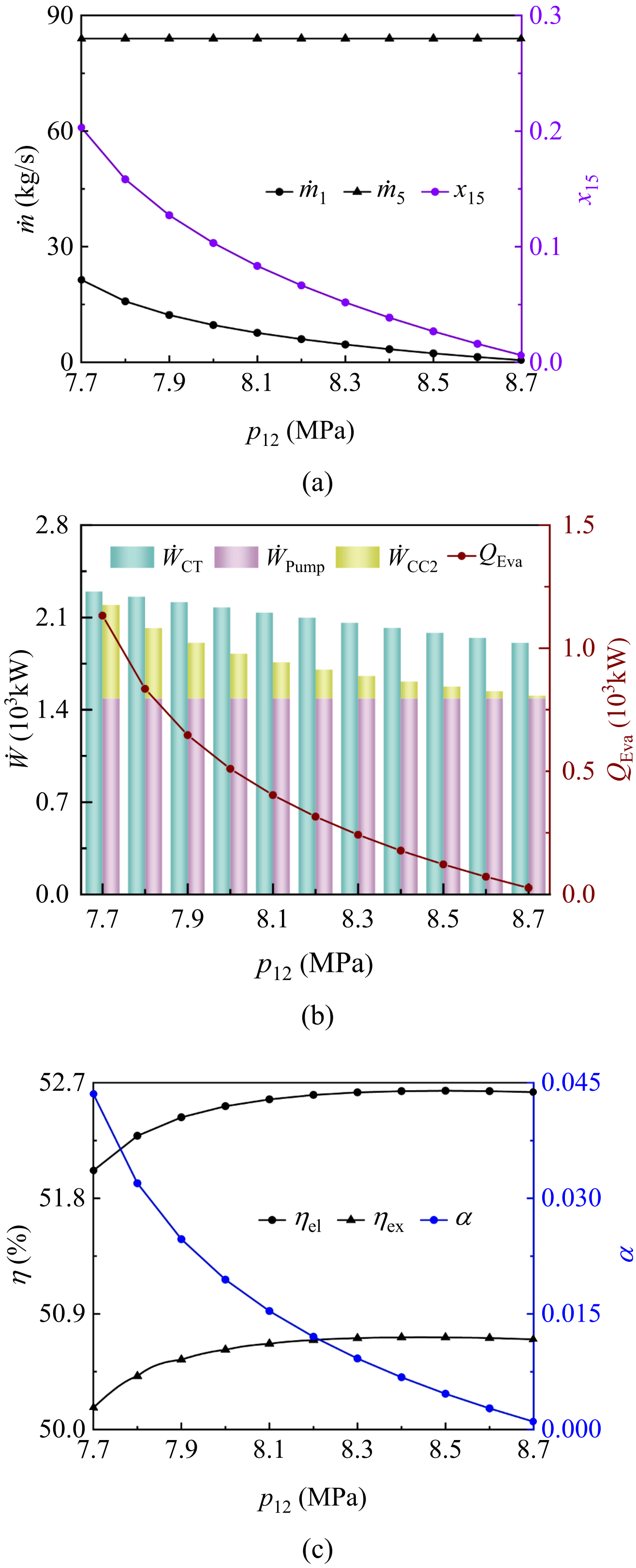

Fig. 8. Influence of CO_2 turbine outlet pressure on system performance.

decreases the vapor composition (x_{15}) at the separator2 inlet from 0.20 to 0.006, thus reducing the refrigeration flow rate of CO_2 by 20.91 kg/s due to the constant power generation flow rate of CO_2. Consequently, as p_{12} rises, the CO_2 turbine power, the CO_2 compressor2 power, and the refrigeration capacity all decline while the pump power consumption remains unchanged, as confirmed in Fig. 8(b). Because the reduction amplitude of the compression work is from a greater to a less than the reduction amplitude of the expansion work, the electrical and exergy efficiencies of the system first increase and then decrease, peaking at 52.64 % and 50.72 % at 8.5 MPa, respectively, as presented in Fig. 8(c).

The reduction in evaporator power by 1.11 MW lowers the system's cooling-to-electricity power ratio from 0.044 to 0.001.

4.3. Optimization and comparison of performance

As obtained from the above parameter analysis, there are optimal values for reactor pressure, air reactor temperature, pump outlet pressure, and CO_2 turbine outlet pressure to maximize system efficiency, underscoring the importance of optimization. Moreover, the system's efficiency and cooling-to-electricity power ratio exhibit global mutual constraints with the changes of fuel reactor temperature and CO_2 turbine outlet pressure, and local mutual constraints with the changes of other design parameters. To acquire the optimal system efficiency and balance it with the cooling-to-electricity power ratio, an NSGA-II-based multi-objective optimization is conducted. Given the nearly synchronous variation of electrical and exergy efficiencies observed in the parameter analysis, electrical efficiency, which is directly related to net electrical power, is selected as one of the objective functions. The decision variable and optimization space are respectively composed of the studied five parameters and their corresponding intervals. The algorithm's parameter settings and the determination of the LINMAP-based Pareto-optimal solution are consistent with the methodology outlined in Ref. [37].

Derived from the multi-objective optimization of the system's CCP performance, the Pareto frontier is displayed in Fig. 9. This frontier represents a series of non-dominated solutions, delineating the optimal cogeneration design boundary of the system. It facilitates rapid identification of the most suitable design scheme based on varying scenario requirements. The labeled solutions A, B, and C denote the highest electrical efficiency, largest cooling-to-electricity power ratio, and Pareto optimality closest to the ideal solution, respectively. The decision variables and system performance metrics for these design schemes are detailed in Table 8. The system's cooling capacity ranges from 187.69 kW to 1386.02 kW, corresponding to a power generation capacity of 26473.26 kW to 24374.36 kW. As the system shifts from the scenario of maximum power generation to that of maximum cooling capacity, the electrical and exergy efficiencies decrease from 52.95 % and 51.02 % to 48.75 % and 47.03 %, respectively, while the cooling-to-electricity power ratio increases from 0.01 to 0.06. The optimal trade-off yields an electrical efficiency of 52.03 %, an exergy efficiency of 50.18 %, and a cooling-to-electricity power ratio of 0.04. The decision variables for achieving the highest efficiency are within the specified parameter ranges, except the fuel reactor temperature. However, the variables for obtaining the largest cooling-to-electricity power ratio are situated at the bounds of these intervals. Expanding the parameter ranges further to increase the cooling-to-electricity power ratio poses several challenges: lower reactor temperatures and pressures can reduce the reaction rate, resulting in incomplete fuel conversion and hindered oxygen carrier regeneration; higher pump outlet pressures exacerbate turbine design complexities due to increased expansion ratios; and lower CO_2 turbine outlet pressures can cause the working medium to transition into the subcritical region, resulting in low efficiency and significant friction losses of the turbine, thus beyond the applicable range of the system.

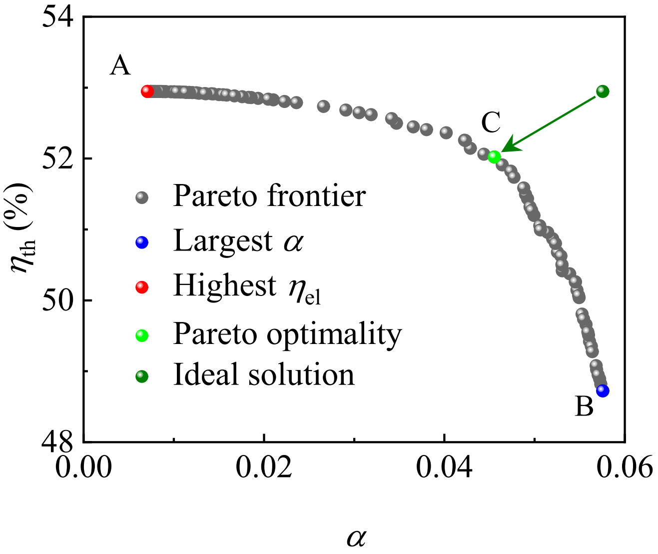

Fig. 9. Pareto frontier for CCP performance of the proposed system.

Table 8
Single-objective and bi-objective optimal performance of the system.

Items	Solution A	Solution B	Solution C
$p_{reactor}$, (MPa)	0.24	0.20	0.21
T_{FR}, (°C)	900.00	800.00	900.00
T_{AR}, (°C)	920.16	850.00	865.86
p_6, (MPa)	16.45	20.00	16.36
p_{12}, (MPa)	8.37	7.70	7.70
$\dot{W}_{net}$, (kW)	26473.26	24374.36	26015.43
$\dot{W}_{cooling}$, (kW)	187.69	1386.02	1169.08
$\dot{E}_{cooling}$, (kW)	4.89	36.10	30.45
η_{el}, (%)	52.95	48.75	52.03
η_{ex}, (%)	51.02	47.03	50.18
α	0.01	0.06	0.04

5. Conclusions

In this study, a novel dual-throttled self-condensing tCO_2 cycle is designed to recover the waste heat from a copper-based CLC power system, aiming to achieve high-efficiency CCP generation. After developing the mathematical model, performance comparisons, exergy analysis, and parametric studies are implemented to assess the cogeneration characteristics of the system. Subsequently, a multi-objective optimization is performed to balance the system's power generation efficiency and cooling-to-electricity power ratio. The following critical conclusions are obtained:

(1) Under base design conditions, the dual-throttle mode with CCP effect reduces the system's electrical and exergy efficiencies by 1.25 and 1.15 percentage points, respectively, compared to the power generation-only single-throttle mode. The components with relatively large exergy destruction are the two reactors and two regenerators in the upstream cycle, and the cooler2, CO_2 pump and low-pressure throttle valve in the downstream cycle.

(2) The optimal reactor operating pressure, air reactor temperature, CO_2 turbine outlet pressure, and pump outlet pressure exist to maximize the system's thermodynamic efficiency. Lowering the operating pressures and temperatures of the two reactors, increasing the pump outlet pressure, and decreasing the CO_2 turbine outlet pressure can enhance the system's cooling capacity.

(3) The increase in the system's generating capacity is synchronized with a decrease in the cooling capacity, leading to mutual constraints on the electrical efficiency and the cooling-to-electricity power ratio. The optimal trade-off performance is characterized by an electrical efficiency of 52.02 %, an exergy efficiency of 50.17 %, and a cooling power of 1169.08 kW.

While the dual-throttle self-condensing tCO_2 cycle has been inspirationally proposed to achieve CCP generation by recovering low-grade waste heat, its limited cooling-to-electricity power ratio restricts its potential applications. Future work should focus on enhancing the system's cooling capacity without compromising efficiency. Meanwhile, an off-design performance investigation is needed to explore effective operational strategies that balance supply and demand. Additionally, the dynamic characteristics of the system are worth exploring when considering the influence of chemical reaction rates.

Declaration of competing interest

The authors declare that they have no known competing financial interests or personal relationships that could have appeared to influence the work reported in this paper.

Acknowledgements

This study is supported by the National Natural Science Foundation of China (Grant No. 52276028) and is undertaken at the Turbomachinery Institute of Beijing Institute of Technology, China.

Data availability

Data will be made available on request.

References

[1] Q. Hassan, P. Viktor, T.J. Al-Musawi, et al., The renewable energy role in the global energy transformations, Renew. Energy Focus 48 (2024) 100545.

[2] S. Anderson, R. Newell, Prospects for carbon capture and storage technologies, Annu. Rev. Environ. Resour. 29 (1) (2004) 109–142.

[3] C. Kunze, H. Spliethoff, Assessment of oxy-fuel, pre-and post-combustion-based carbon capture for future IGCC plants, Appl. Energy 94 (2012) 109–116.

[4] S. Daneshmand-Jahromi, M.H. Sedghkerdar, N. Mahinpey, A review of chemical looping combustion technology: fundamentals, and development of natural, industrial waste, and synthetic oxygen carriers, Fuel 341 (2023) 127626.

[5] J. Adanez, A. Abad, F. Garcia-Labiano, et al., Progress in chemical-looping combustion and reforming technologies, Prog. Energy Combust. Sci. 38 (2) (2012) 215–282.

[6] A. Lyngfelt, B. Leckner, T. Mattisson, A fluidized-bed combustion process with inherent CO_2 separation; application of chemical-looping combustion, Chem. Eng. Sci. 56 (10) (2001) 3101–3113.

[7] F. Güleç, J.A. Okolie, Decarbonising bioenergy through biomass utilisation in chemical looping combustion and gasification: a review, Environ. Chem. Lett. 22 (1) (2024) 121–147.

[8] M. Ishida, D. Zheng, T. Akehata, Evaluation of a chemical-looping-combustion power-generation system by graphic exergy analysis, Energy 12 (2) (1987) 147–154.

[9] L. Liu, H. Cao, Technical and life cycle performance comparison between petroleum coke chemical looping combustion and oxy-combustion combining with advanced steam cycles for power generation processes, J. Clean. Prod. 417 (2023) 137960.

[10] W. Chan, T. Morosuk, X. Li, et al., Allam cycle: Review of research and development, Energ. Conver. Manage. 294 (2023) 117607.

[11] C.C. Cormos, Assessment of copper-based chemical looping air separation system for energy efficiency improvements of oxy-combustion and gasification power plants, Appl. Therm. Eng. 130 (2018) 120–126.

[12] S. Saqline, L. Yang, A. Romagnoli, et al., Coupling chemical looping air separation with the Allam cycle–A thermodynamic analysis, J. Clean. Prod. 418 (2023) 138097.

[13] Z. Liu, Z. Li, Y. Zhang, et al., Thermodynamic analysis of using chemical-looping combustion in Allam-Z cycle instead of common combustion, Energ. Conver. Manage. 254 (2022) 115229.

[14] S. Zhang, L. Li, E. Huo, et al., Parameters analysis and techno-economic comparison of various ORCs and sCO_2 cycles as the power cycle of Lead–Bismuth molten nuclear micro-reactor, Energy 295 (2024) 131103.

[15] W. Cu, J. Fang, X. Guo, et al., Investigation of thermodynamic performances of particle/supercritical CO_2 fluidized bed heat exchanger integrated with supercritical CO_2 recompression Brayton cycle for concentrated solar power, Energ. Conver. Manage. 315 (2024) 118805.

[16] Z. Fang, Z. Liu, S. Zhang, et al., Performance evaluation and multi-objective optimization of a solar-thermal-assisted energy system: supercritical CO_2 Brayton cycle and solid oxide electrolysis/fuel cells, Energ. Conver. Manage. 308 (2024) 118404.

[17] Y. Liang, W. Chen, X. Luo, et al., Multi-objective optimization of supercritical CO_2 Brayton cycles for coal-fired power generation with two waste heat recovery schemes, Energ. Conver. Manage. 300 (2024) 117962.

[18] N. Khallaghi, D.P. Hanak, V. Manovic, Gas-fired chemical looping combustion with supercritical CO_2 cycle, Appl. Energy 249 (2019) 237–244.

[19] Y. Wang, L. Zhu, Y. He, et al., Comparative exergoeconomic analysis of atmosphere and pressurized CLC power plants coupled with supercritical CO_2 cycle, Energy 265 (2023) 126401.

[20] Y. Du, Z. Yu, C. Yang, et al., Techno-economic optimization of the combined supercritical carbon dioxide and air brayton cycles driven by copper-based chemical looping combustion, Energy Fuel 38 (3) (2024) 2305–2318.

[21] Y. Wang, L. Zhu, Y. He, et al., Tech-economic assessment of chemical looping combustion coupled with the combined supercritical CO_2 Brayton cycle and ORC for power generation, J. Taiwan Inst. Chem. Eng. 129 (2021) 197–206.

[22] Y. Du, Z. Yu, W. Sun, et al., Chemical looping combustion-driven cooling and power cogeneration system with LNG cold energy utilization: exergoeconomic analysis and three-objective optimization, Energy 295 (2024) 130877.

[23] Z. Ma, J. Wang, F. Dong, et al., Thermodynamic analysis of fuel-cell-based combined cooling, heating, and power system integrated solar energy and chemical looping hydrogen generation, Energy 238 (2022) 121974.

[24] L. Pan, B. Li, W. Shi, et al., Optimization of the self-condensing CO_2 transcritical power cycle using solar thermal energy, Appl. Energy 253 (2019) 113608.

[25] M.Z. Haq, M.S.R. Ayon, M.W.B. Nouman, et al., Thermodynamic analysis and optimisation of a novel transcritical CO_2 cycle, Energ. Conver. Manage. 273 (2022) 116407.

[26] T.H. Cetin, J. Zhu, Thermodynamic assessment of a novel self-condensing sCO_2 recompression system with vortex tube, Energ. Conver. Manage. 269 (2022) 116110.

[27] Y. Wan, C. Wu, C. Liu, et al., A novel self-condensing transcritical CO_2 power cycle with a vortex tube: thermoeconomic assessment study and comparison, Energ. Conver. Manage. 286 (2023) 117026.

[28] K. Chen, S. Liang, Z. Shen, et al., Thermodynamic assessment of a novel and efficient self-condensing transcritical CO_2 power cycle with a vortex tube, Appl. Therm. Eng. 245 (2024) 122825.

[29] J. Xia, J. Wang, J. Lou, et al., Thermodynamic, economic analysis and multi-objective optimization of an improved self-condensing transcritical CO_2 Rankine cycle with two-stage ejector for low grade heat utilization, Energ. Conver. Manage. 305 (2024) 118259.

[30] Y. Guo, X. Guo, J. Wang, et al., Comprehensive analysis and optimization for a novel combined heating and power system based on self-condensing transcritical CO_2 Rankine cycle driven by geothermal energy from thermodynamic, exergoeconomic and exergoenvironmental aspects, Energy 300 (2024) 131581.

[31] Z. Liu, Z. Liu, X. Xuann, et al., Proposal and assessment of a novel carbon dioxide energy storage system with electrical thermal storage and ejector condensing cycle: energy and exergy analysis, Appl. Energy 269 (2020) 115067.

[32] G. Liu, G. Lisak, Cu-based oxygen carriers for chemical looping processes: opportunities and challenges, Fuel 342 (2023) 127828.

[33] I. Adanez-Rubio, M. Arjmand, H. Leion, et al., Investigation of combined supports for Cu-based oxygen carriers for chemical-looping with oxygen uncoupling (CLOU), Energy Fuel 27 (7) (2013) 3918–3927.

[34] E.W. Lemmon, M.L. Huber, M.O. McLinden, NIST reference fluid thermodynamic and transport properties–REFPROP, NIST Standard Reference Database 2002 (23) (2002) v7.

[35] A. Bejan, G. Tsatsaronis, M.J. Moran. Thermal design and optimization, John Wiley & Sons, 1995.

[36] A. Edrisi, Z. Mansoori, B. Dabir, et al., Hydrogen, nitrogen and carbon dioxide production through chemical looping using iron-based oxygen carrier–A Green plant for H2 and N2 production, Int. J. Hydrogen Energy 39 (20) (2014) 10380–10391.

[37] Y. Du, L. Wang, Z. Yu, et al., Multi-objective optimization of thermoeconomic and component size of supercritical carbon dioxide recompression cycle based on small-scale lead-cooled fast reactor, Int. J. Energy Res. 46 (10) (2022) 13570–13589.